


 Cite this: *Phys. Chem. Chem. Phys.*,  
2026, **28**, 4412

# High-resolution spectroscopy of $[\text{H,C,N}]^+$ : III. Infrared $\tilde{\text{A}}^2\Sigma^+ \leftarrow \tilde{\text{X}}^2\Pi$ electronic transition of $\text{HCN}^+$

 Samuel J. P. Marlton,<sup>1</sup> Philipp C. Schmid,<sup>2</sup> Wesley G. D. P. Silva,<sup>3</sup> Oskar Asvany<sup>1</sup> and Stephan Schlemmer<sup>1\*</sup>

 Received 4th November 2025,  
Accepted 9th December 2025

DOI: 10.1039/d5cp04255k

rsc.li/pccp

The  $\tilde{\text{A}}^2\Sigma^+ \leftarrow \tilde{\text{X}}^2\Pi$  electronic transition of the fundamental  $\text{HCN}^+$  ion is reported. The spectrum exhibits a rotational, fine, and hyperfine structure that provides insights into the geometries and wavefunctions of the  $\tilde{\text{A}}^2\Sigma^+$  and  $\tilde{\text{X}}^2\Pi$  states. The extracted spectroscopic constants for the  $\tilde{\text{A}}$  state include (in  $\text{cm}^{-1}$ )  $T_e = 3238.8224(2)$ ,  $B = 1.39568(3)$ ,  $D = 2.27(9) \times 10^{-5}$ ,  $\gamma = -0.07332(7)$ ,  $\gamma_D = 1.87(3) \times 10^{-4}$ , and the Fermi contact hyperfine constant for the  $\text{HCN}^+$  nitrogen atom  $b_F = 0.0059(1)$ . Based on this value, the  $\tilde{\text{A}}^2\Sigma_{1/2}^+$  state electronic wavefunction is estimated to have  $11.5 \pm 0.2\%$  s orbital character. The spin-orbit coupling constant for the  $\tilde{\text{X}}$  state was also determined with high precision  $A_{\text{SO}} = -49.3122(4) \text{ cm}^{-1}$ . This work illustrates that leak-out spectroscopy can be applied to measure high-resolution spectra of low energy electronic transitions.

## Introduction

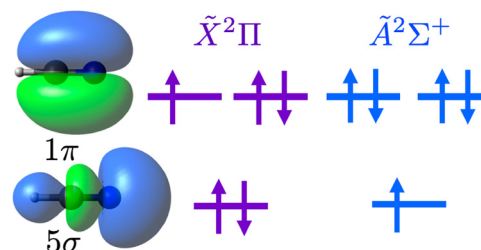
The  $\text{HCN}^+$  cation is a fundamental molecule with an interesting electronic structure; however, limited details have been reported about its electronic excited states.  $\text{HCN}^+$  is highly reactive,<sup>1,2</sup> making it difficult to isolate for spectroscopic interrogation, so the only reported infrared spectra of  $\text{HCN}^+$  are vibrational spectra in inert Ne matrices<sup>3</sup> and rovibrational and rotational spectra that have recently been measured in cryogenic ion traps as part of this series of publications.<sup>4,5</sup>

No electronic transitions of  $\text{HCN}^+$  have been directly measured; however, individual states of  $\text{HCN}^+$  have been observed by photoionisation and photoelectron spectroscopy of the less reactive neutral  $\text{HCN}$ .<sup>6–10</sup> In these investigations, several bands from the  $\text{HCN}^+ \tilde{\text{X}}^2\Pi$  ground state and a low lying  $\tilde{\text{A}}^2\Sigma^+$  state were observed. These states are separated by only  $\approx 3250 \text{ cm}^{-1}$  because of the similar energies of the  $1\pi$  and  $5\sigma$  orbitals, which are illustrated in Fig. 1.<sup>6–10</sup>

In most of these photoelectron and photoionisation spectra, only vibronic transitions are resolved.<sup>7–10</sup> The highest resolution was achieved using zero electron kinetic energy (ZEKE) photoionisation spectroscopy ( $\Delta\bar{\nu} = 1 \text{ cm}^{-1}$ ), which exhibited a partially resolved rotational structure.<sup>6</sup> From the ZEKE spectra, it was possible to extract first experimental values of spin-orbit coupling of the ground state ( $A_{\text{SO}} = -49.8(1) \text{ cm}^{-1}$ ), the rotational constant of the  $\tilde{\text{X}}^2\Pi$  ground state ( $B' = 1.36(1) \text{ cm}^{-1}$ ), and the rotational constant of the  $\tilde{\text{A}}^2\Sigma^+$  excited state

( $B' = 1.37(1) \text{ cm}^{-1}$ ). Despite being high-quality spectra, it is not clear from these results whether the rotational constant significantly changes in the  $\tilde{\text{A}}^2\Sigma^+$  excited state. This is in contrast to high-level multireference configuration interaction calculations that include vibronic coupling, which predict a significant excited state CN bond contraction, which significantly changes the rotational constant in the excited state.<sup>11</sup> Furthermore, higher resolution experimental studies are required to characterise the more subtle spectroscopic properties of  $\text{HCN}^+$ . For example, the couplings between electronic orbital angular momentum ( $\Lambda$ ), electron spin ( $S$ ), nuclear rotation, and nuclear spin of the nitrogen ( $I_{\text{N}}$ ) and hydrogen ( $I_{\text{H}}$ ) are of fundamental interest.

In particular, the hyperfine coupling between electronic angular momenta and nuclear spin is valuable because it facilitates quantitative experimental characterisation of the electronic wavefunction.<sup>12</sup> Some of these couplings have now been described for the  $\tilde{\text{X}}^2\Pi$  state vibrational levels,<sup>4,5</sup> but not for excited electronic states. The ability to characterise these subtle couplings in the excited state is also a necessary step


 Fig. 1 Relevant molecular orbitals of  $\text{HCN}^+$ .

<sup>1</sup> *Physikalisches Institut, Universität zu Köln, Zùlpicher Str. 77, 50937 Cologne, Germany. E-mail: marlton@ph1.uni-koeln.de, schlemmer@ph1.uni-koeln.de*



towards finding promising candidate polyatomic molecular ions for which laser-cooling might be possible.<sup>13</sup>

It is often challenging to characterise the more subtle couplings between angular momenta for gas-phase ions in excited electronic states. For example, hyperfine splitting in excited electronic states is typically on the order of less than  $0.1 \text{ cm}^{-1}$  and has been observed for only a few gas-phase molecular ions, almost all of which are diatomics.<sup>14–24</sup> To our knowledge, the only polyatomic ions for which excited state hyperfine splitting has been observed in the gas-phase are isotopologues of  $\text{HCP}^+$  and  $\text{N}_2\text{O}^+$ .<sup>22,23</sup> One reason for this is that excited electronic states often have picosecond or femtosecond lifetimes, and so lifetime broadening makes small splittings between rovibronic lines unresolvable.<sup>25</sup> Lifetime broadening becomes an increasingly common feature of larger molecules because they have more degrees of freedom and higher densities of states, which can facilitate fast excited state deactivation by dissociation, internal conversion, or intersystem crossing.

Well established methods for measuring electronic spectra of gas-phase ions are generally not suitable for resolving splittings smaller than  $0.01 \text{ cm}^{-1}$ . For example, single-photon resonance enhanced photodissociation spectroscopy is often lifetime broadened,<sup>25</sup> one-colour multiphoton dissociation can produce broad peaks that are slightly shifted,<sup>26,27</sup> messenger tagging does not provide a spectrum of the bare ion,<sup>28–30</sup> and one-colour photoionisation spectroscopy of neutral precursors with high energy photons is more Doppler broadened because this broadening increases proportionally to the photon energy. High-resolution infrared spectra of the  $\text{HCN}^+ \tilde{A}^2\Sigma^+ \leftarrow \tilde{X}^2\Pi$  transition are probably achievable using techniques such as laser induced reactions (LIR),<sup>31</sup> laser induced inhibition of cluster growth (LIICG),<sup>32</sup> and multiple-colour spectroscopy.<sup>29,30</sup> However, these methods typically require sophisticated understanding of some reaction schemes, spectroscopic levels, or subtle experimental conditions to implement. Finally, ions like  $\text{HCN}^+$  are too reactive to be straightforwardly investigated in jets, discharges, and absorption cells.

In this study, we show that the recently developed leak-out spectroscopy (LOS) method<sup>33</sup>—which was recently applied to electronic spectroscopy for the first time<sup>34</sup>—overcomes some of these disadvantages and yields a high resolution single photon electronic spectrum of bare  $\text{HCN}^+$ . This is the first spectrum of the  $\tilde{A}^2\Sigma^+ \leftarrow \tilde{X}^2\Pi$  transition for  $\text{HCN}^+$ , and the spectrum has a sufficiently high resolution to resolve a rotational, fine, and hyperfine structure. This is encouraging for the potential to measure single-photon electronic spectra of bare gas-phase ions far below the dissociation threshold using leak-out spectroscopy.

This article is a part of a series of publications reporting high-resolution infrared rovibrational<sup>4</sup> and pure rotational<sup>5</sup> spectra of  $\text{HCN}^+$ . The previous parts of this series described the couplings between electronic and nuclear angular momenta of  $\text{HCN}^+$  in the  $\tilde{X}$  electronic state. The electronic spectrum of this work was shown in Publication I of this series without analysis.<sup>4</sup> In this part, we describe the couplings between electronic and nuclear angular momenta of  $\text{HCN}^+$  in the  $\tilde{X}$  and  $\tilde{A}$  states. We then discuss the rovibronic structure of the experimental  $\tilde{A}^2\Sigma^+ \leftarrow \tilde{X}^2\Pi$  LOS

spectrum. The experimental spectrum is fitted with a rovibronic Hamiltonian to extract several spectroscopic constants. These results are contextualised by comparison with a calculated potential energy surface. We then discuss the hyperfine splitting observed in the  $\tilde{A}^2\Sigma^+ \leftarrow \tilde{X}^2\Pi$  spectrum, which provides further insights into the electronic wavefunction of the  $\text{HCN}^+ \tilde{A}$  state. Finally, we report a further rovibrational transition of  $\text{HCN}^+$  that overlaps with the rovibronic  $\tilde{A}^2\Sigma^+ \leftarrow \tilde{X}^2\Pi$  spectrum. We argue that this rovibrational transition excites an upper ( $\kappa$ ) Renner–Teller component of an  $\tilde{X}$  state combination band composed of two quanta of  $\nu_2$  and one quantum of  $\nu_1$ . Together with the previous studies and the earlier parts of this series,<sup>4–6,11</sup> these results provide a detailed experimental foundation for understanding the Renner–Teller vibronic coupling in  $\text{HCN}^+$ , as well as the vibronic, rovibronic, fine, and hyperfine structure of the  $\text{HCN}^+ \tilde{A}$  electronic state.

## Experimental details

Spectra were measured using leak-out spectroscopy (LOS) in the cryogenically cooled 22-pole ion trap instrument referred to as LIRtrap.<sup>31,35</sup> This method has been described in detail previously.<sup>33</sup> Briefly,  $\text{HCN}^+$  ions were generated from acetonitrile vapour, which were bombarded with 70 eV electrons in a storage ion source. The ions in the source were pulsed out every 500 ms into a quadrupole mass filter (QMF1), which was set to select  $m/z$  27. The mass selected ions exiting the QMF1 were then trapped and stored in a 22-pole ion trap mounted on a 10 K cold-head.<sup>36</sup> After 10 ms of cooling with the neutral Ne (with a continuous number density of approximately  $10^{14} \text{ cm}^{-3}$ ) in the trap region, the ions were irradiated by light from a continuous optical parametric oscillator system (Toptica TOPO,  $\approx 100 \text{ W cm}^{-2}$ , accuracy  $\approx 10^{-4} \text{ cm}^{-1}$ ) for 300 ms, the timing of which was controlled with a mechanical shutter. The light frequency was measured using a wavemeter (Bristol 621 A-IR, resolution  $\approx 10^{-3} \text{ cm}^{-1}$ ). Photo-excited ions could collide with neutral Ne buffer gas to convert some of their internal energy into kinetic energy. The ions with enhanced kinetic energy could overcome the low potential barrier at the trap exit and leak out of the trap. After exiting the trap, ions pass through a second quadrupole mass filter (QMF2) set to select  $m/z$  27, before being detected using a Daly type detector.<sup>37,38</sup> This process was repeated while scanning the OPO frequency to record a rovibrational LOS spectrum.

Several experimental configurations that differed slightly from one another were employed in this study. The spectrum was measured at a trap temperature of 27 K with continuous Ne as the buffer gas ( $n \approx 2 \times 10^{14} \text{ cm}^{-3}$ ). This configuration was optimised to observe transitions involving the  $\Omega = 1/2$  component of the ground state, which requires elevated temperatures because the  $\Omega = 3/2$  component is lower in energy by  $\approx 50 \text{ cm}^{-1}$ . This configuration was also optimised to suppress background peaks from isobaric  $\text{C}_2\text{H}_3^+$  by lowering the trap potential, which increased the trap strength and reduced the leak-out signal of  $\text{C}_2\text{H}_3^+$  more than that of  $\text{HCN}^+$ . This difference between the leak-out signal of  $\text{C}_2\text{H}_3^+$  and  $\text{HCN}^+$  probably reflects a difference



in their vibrational to kinetic energy transfer characteristics. A small range of the spectrum was measured at 9 K, with a 1 : 3 mixture of Ne:He that was pulsed into the ion trap. This configuration was optimised to provide a contour fit of the hyperfine splitting, which required low temperature to reduce Doppler broadening and care to avoid saturating the transitions as a result of near-total leak-out of the trapped ion population. Finally, the spectrum was remeasured at 4 K, with a 1 : 3 mixture of Ne : He that was pulsed into the ion trap, using the COLtrap machine.<sup>38</sup> This configuration was optimised to provide the line positions of hyperfine components.

### Computational details

The geometries of the  $\tilde{X}^2\Pi$  and  $\tilde{A}^2\Sigma^+$  states were optimised using the CASPT2(9,8)/cc-pVQZ method<sup>39,40</sup> in the OpenMolcas program.<sup>41</sup> The PES in Fig. 4 is constructed by linear interpolation of the xyz coordinates from the optimised  $\tilde{X}^2\Pi$  geometry (interpolated coordinate = 0) to the optimised  $\tilde{A}^2\Sigma^+$  geometry (interpolated coordinate = 1). The electronic energies in Fig. 4 are calculated using the SOC+MRCI+Q(9,8)/cc-pVQZ method<sup>40,42</sup> in the ORCA/5.0.2 program.<sup>43</sup>

## Results and discussion

### Angular momenta and splitting

HCN<sup>+</sup> has a relatively complex electronic structure because it has several angular momenta that couple differently in the  $\tilde{X}$  and  $\tilde{A}$  states. These include the rotation of the nuclear framework  $R$ , electronic orbital angular momentum  $\Lambda$ , electron spin  $S$ , nuclear spin of the nitrogen  $I_N$  and nuclear spin of the hydrogen  $I_H$ . We also refer to the total angular momentum exclusive of electron and nuclear spin  $N$ , the total angular momentum exclusive of nuclear spin  $J$ , the total angular momentum exclusive of the hydrogen nuclear spin  $F_1$  and the total angular momentum  $F$ . The splittings

in the ground  $\tilde{X}$  and excited  $\tilde{A}$  states are illustrated in Fig. 2 for a level with one quantum of nuclear rotation ( $R = 1$ ) and will be discussed with reference to the experimental spectrum.

The couplings between these angular momenta were described in detail in parts 1 and 2 of this series for the  $\tilde{X}$  state,<sup>4,5</sup> and the couplings of a  $\Sigma$  symmetry vibrationally excited state were also described in part 1 of this series.<sup>4</sup> Nevertheless, it will be necessary to describe how these couplings split rovibrational levels in order to understand the experimental spectra reported here.

### Leak-out spectroscopy

The experimental spectrum of the  $\tilde{A}^2\Sigma^+ \leftarrow \tilde{X}^2\Pi$  vibronic origin transition measured using leak-out spectroscopy (LOS) is shown in Fig. 3 (black trace). This spectrum was measured at 27 K. Spin-orbit coupling (SOC) splits the  $\tilde{X}^2\Pi$  state into two components— $\tilde{X}^2\Pi_{3/2}$  and  $\tilde{X}^2\Pi_{1/2}$ —which are distinguished by the quantum number of the total electron angular momentum  $\Omega = |\Lambda + \Sigma| = |1 \pm 1/2|$ , where  $\Lambda$  and  $\Sigma$  are the quantum numbers for the orbital and spin angular momenta associated with  $\hat{L}_z$  and  $\hat{S}_z$ , respectively. The  $\Omega = 3/2$  component is lower in energy because the  $\dots 1\pi^3$  configuration is more than half-filled (Fig. 1). The experimental spectrum exhibits both the  $\tilde{A}^2\Sigma_{1/2}^+ \leftarrow \tilde{X}^2\Pi_{3/2}$  and  $\tilde{A}^2\Sigma_{1/2}^+ \leftarrow \tilde{X}^2\Pi_{1/2}$  components, with the  $\tilde{A}^2\Sigma_{1/2}^+ \leftarrow \tilde{X}^2\Pi_{3/2}$  transition being more intense. The  $\tilde{A}^2\Sigma_{1/2}^+ \leftarrow \tilde{X}^2\Pi_{3/2}$  transition is recognisable as a  $\Omega = 1/2 \leftarrow 3/2$  type transition because there are no transitions involving  $J'' = 1/2$ , but there are transitions involving  $J' = 1/2$ .

Coupling of the angular momenta of HCN<sup>+</sup> split the rovibronic levels of the ground and excited state, as summarised in Fig. 2. For the  $\tilde{X}^2\Pi$  state, the largest splitting arises from spin orbit coupling, giving rise to  $\tilde{X}^2\Pi_{1/2}$  and  $\tilde{X}^2\Pi_{3/2}$  components with a spin-orbit constant of  $A_{SO} = -49.3122(4) \text{ cm}^{-1}$  (indicated in Fig. 3). This value is reasonably close to previous MRCI calculations ( $-49.9 \text{ cm}^{-1}$ )<sup>11</sup> and ZEKE measurements ( $-49.8 \text{ cm}^{-1}$ )<sup>6</sup> and  $-49.3113(3) \text{ cm}^{-1}$  calculated from the rovibrational spectra reported in part I of this series.<sup>4</sup> Each  $J$  rotational level in the  $\tilde{X}^2\Pi$  state is split by

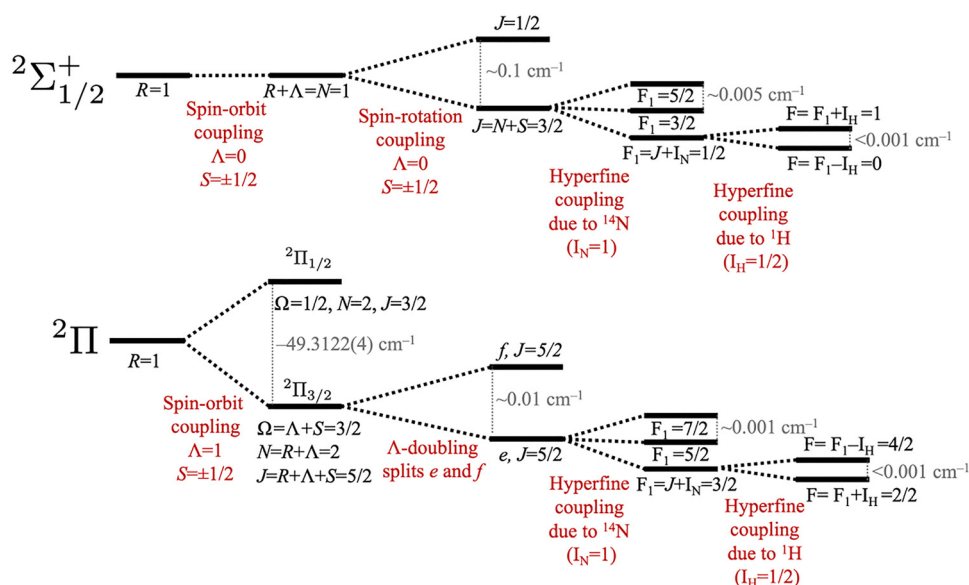


Fig. 2 Summary of relevant splittings for HCN<sup>+</sup>.



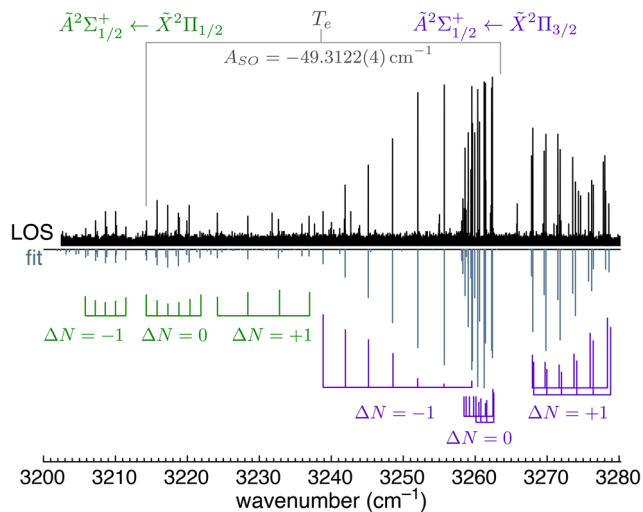


Fig. 3 Electronic spectrum of the  $\text{HCN}^+ \tilde{A}^2\Sigma^+ \leftarrow \tilde{X}^2\Pi$  origin transition (black trace) measured using LOS at 27 K compared with a simulation (grey sticks) based on a fit using the PGOPHER program.<sup>44</sup>

$\Lambda$ -doubling into e and f components. The  $\tilde{A}^2\Sigma^+$  state does not split by spin orbit coupling because it has  $\Lambda = 0$ . However, the spin ( $S = 1/2$ ) couples with nuclear rotation to split each  $N$  rotational level into two components with  $J = |N \pm S|$ . Additional splitting from hyperfine coupling will be discussed later.

These couplings between nuclear rotation and electronic angular momenta give rise to a level structure that is shown in the SI, which also illustrates the various possible branches that are observed in the rovibronic spectrum. The selection rules are  $\Delta J = 0, \pm 1$ , with  $e \leftrightarrow f$  for  $\Delta J = 0$  or  $e \leftrightarrow e$  and  $f \leftrightarrow f$  for  $\Delta J = \pm 1$ . This means that there are six branches expected for the  $\tilde{A}^2\Sigma_{1/2}^+ \leftarrow \tilde{X}^2\Pi_{3/2}$  transition and six branches for the  $\tilde{A}^2\Sigma_{1/2}^+ \leftarrow \tilde{X}^2\Pi_{1/2}$  transition, which we label by  $\Delta N$  (in lower case) and  $\Delta J$  (in upper case). Eleven of these twelve branches were observed, with the exception of the weak oP branch ( $\Delta N = -2$  and  $\Delta J = -1$ ) of the  $\tilde{A}^2\Sigma_{1/2}^+ \leftarrow \tilde{X}^2\Pi_{1/2}$  transition. The observed branches were included in a global fit with a nearby  $\text{HCN}^+$  combination band of  $\Pi$  symmetry that has not been reported before, with the rovibrational  $\nu_1$  spectrum reported in ref. 4, the rovibrational spectrum of a combination band with  $\Sigma$  symmetry reported in ref. 4, and the rotational spectra reported in ref. 5. We refer to this fit as “fit 1”, which does not include hyperfine coupling. The observed rovibronic and rovibrational lines of  $\text{HCN}^+$  are captured well by fit 1, with average residuals lower than the wavemeter resolution ( $0.001 \text{ cm}^{-1}$ ). Additional lines are observed that arise from isobaric  $\text{C}_2\text{H}_3^+$ .

The experimental spectrum in Fig. 3 is compared to a fit produced using the PGOPHER program<sup>44</sup> using the Hamiltonian:

$$\begin{aligned} \hat{H}_{\text{rve}} = & T_e + A_{\text{SO}} \hat{L}_z \hat{S}_z + B \hat{N}^2 - D \hat{N}^4 + \gamma \hat{N} \cdot \hat{S} + \frac{1}{2} \gamma_{\text{D}} [\hat{N} \cdot \hat{S}, \hat{N}^2]_+ \\ & - \frac{1}{2} p (\hat{N}_+ \cdot \hat{S}_+ e^{-2i\phi} + \hat{N}_- \cdot \hat{S}_- e^{+2i\phi}) \\ & + \frac{1}{2} q (\hat{N}_+^2 e^{-2i\phi} + \hat{N}_-^2 e^{+2i\phi}) \end{aligned} \quad (1)$$

where  $N$  is the total angular momentum without nuclear spin or electron spin,  $S$  is the electron spin,  $L$  is the electron angular momentum,  $T_e$  is the term energy,  $A_{\text{SO}}$  is the spin-orbit coupling constant,  $B$  is the rotational constant,  $D$  is the centrifugal distortion constant,  $\gamma$  is the spin-rotation coupling constant,  $\gamma_{\text{D}}$  is the spin-rotation distortion constant, and  $p$  and  $q$  are the  $\Lambda$  doubling constants.

The spectroscopic constants from fit 1 are shown in Table 1. The  $B$  rotational constant is 3% larger in the  $\tilde{A}$  state ( $B' = 1.39581(3) \text{ cm}^{-1}$ ) than in the  $\tilde{X}$  state ( $B' = 1.35276(2) \text{ cm}^{-1}$ ). This result is in good agreement with the  $B$  constants from sophisticated MRCI calculations that take into account vibronic coupling ( $B' = 1.3974 \text{ cm}^{-1}$  and  $B'' = 1.3533 \text{ cm}^{-1}$ ).<sup>11</sup> This agreement also indicates that the  $\tilde{A}$  state is mixed with the excited  $(\nu_1 + \nu_2)\mu$  vibrational level of the  $\tilde{X}^2\Pi$  ground state and that vibronic mixing beyond the Born-Oppenheimer approximation is particularly important for  $\text{HCN}^+$ , as calculated in ref. 11. Because the rotational constant  $B$  is determined by the moment of inertia, which is determined by the molecular structure, these values validate the calculated result that the CN bond distance contracts significantly in the  $\tilde{A}$  state. Based on previous ZEKE experiments, it was ambiguous whether the CN bond length significantly contracts in the excited state ( $B' = 1.37(1) \text{ cm}^{-1}$  and  $B'' = 1.36(1) \text{ cm}^{-1}$ ).<sup>6</sup> This ambiguity between experiment and theory is now resolved by the higher resolution spectra presented here.

To illustrate the electronic states and their geometry changes investigated in this work, a potential energy surface (PES) for  $\text{HCN}^+$  is shown in Fig. 4. The PES follows the  $\tilde{X}^2\Pi_{3/2}$  (purple curve) and  $\tilde{X}^2\Pi_{1/2}$  (green curve) spin-orbit components of the ground electronic state and the  $\tilde{A}^2\Sigma^+$  excited state (blue curve). The  $x$  axis in Fig. 4 shows the optimised  $\tilde{X}$  state geometry at  $x = 0$  and the optimised  $\tilde{A}$  state geometry at  $x = 1$ . Other  $x$  axis values represent interpolation (or extrapolation) between the  $xyz$  coordinates of the  $\tilde{X}$  and  $\tilde{A}$  optimised geometries. Both states have linear  $C_{\infty v}$  optimised geometries, and the CH bond length is similar in the  $\tilde{X}$  ground state ( $\text{CH}_{\tilde{X}} = 1.087 \text{ \AA}$ ) and the  $\tilde{A}$  excited state ( $\text{CH}_{\tilde{A}} = 1.086 \text{ \AA}$ ). The calculated CN bond length is much larger in the  $\tilde{X}$  ground state ( $\text{CN}_{\tilde{X}} = 1.222 \text{ \AA}$ ) than in the  $\tilde{A}$  excited state ( $\text{CN}_{\tilde{A}} = 1.150 \text{ \AA}$ ). Based on our calculations, the  $\tilde{A}^2\Sigma^+ \leftarrow \tilde{X}^2\Pi$  origin transition can be expected to be weak because of a low oscillator strength ( $f = 0.0004$  as calculated using MRCI+Q) and unfavorable Franck-Condon factors due to the change in the CN bond distance.

There is an avoided crossing between the  $\tilde{A}^2\Sigma_{1/2}^+$  state and the  $\tilde{X}^2\Pi_{1/2}$  component close to the  $\tilde{A}^2\Sigma_{1/2}^+$  state minimum (see Fig. 4b), which involves the two states repelling each other and exchanging electronic character due to SOC (note that the selection rule for spin-orbit interactions between electronic states is  $\Delta\Omega = 0$ ). Although the states do not cross, the lower energy  $\Omega = 1/2$  state has  $\tilde{A}^2\Sigma_{1/2}^+$  character at  $\text{CN} = 1.132 \text{ \AA}$ , the higher energy  $\Omega = 1/2$  state has  $\tilde{A}^2\Sigma_{1/2}^+$  character at  $\text{CN} = 1.138 \text{ \AA}$ , and the electronic character of both states is mixed at  $\text{CN} = 1.1355 \text{ \AA}$  as visualised by the changing colour in Fig. 4b. Although this avoided crossing is close to the minimum of the  $\tilde{A}^2\Sigma_{1/2}^+$  state, there are no apparent effects from this avoided



**Table 1** Spectroscopic constants of HCN<sup>+</sup> states determined by a simultaneous fit of the  $\tilde{A}^2\Sigma^+ \leftarrow \tilde{X}^2\Pi$  electronic spectrum, pure rotational transitions, rovibrational spectrum of the fundamental C–H stretch  $\nu_1$ , and the rovibrational spectra of two combination bands— $\nu_3(\sigma) + 2\nu_2(\pi)$  and  $\nu_1(\sigma) + \nu_2(\pi)$ . Fit 1 refers to this global fit. Fit 2 of the  $\tilde{A}$  state refers to a line fit of the 4 K spectrum, which includes hyperfine splitting. The symmetry of single quanta of the  $\nu_1(\sigma)$  and  $\nu_2(\pi)$  vibrations is indicated. All values are reported in cm<sup>-1</sup>. The hyperfine constants from fit 2 are shown in Table 2

|                                | $\tilde{X}^2\Pi$      |                    |                    |                              |                               |                   |
|--------------------------------|-----------------------|--------------------|--------------------|------------------------------|-------------------------------|-------------------|
|                                | Fit 1 <sup>a</sup>    | Fit 2 <sup>a</sup> | Rovib <sup>b</sup> | MRCI <sup>c</sup>            | ZEKE <sup>d</sup>             | Rot <sup>e</sup>  |
| <i>B</i>                       | 1.35276(1)            | 1.35278(2)         | 1.35275(1)         | 1.3533                       | 1.36(1)                       | 1.3527672(2)      |
| <i>A</i>                       | -49.3120(3)           | -49.3122(4)        | -49.3113(3)        | -49.9                        | -49.8(2)                      |                   |
| <i>A<sub>D</sub></i>           | -0.00145(4)           | -0.00146(3)        | -0.00144(1)        |                              |                               |                   |
| <i>p</i>                       | 0.0245(1)             | 0.0250(1)          | 0.02440(6)         |                              |                               |                   |
| <i>q</i>                       | -0.00201(1)           | -0.001995(6)       | -0.002001(6)       |                              |                               | -0.0020026(3)     |
| <i>D</i> (× 10 <sup>-6</sup> ) | 3.3(2)                | 3.1(4)             | 3.3(1)             |                              |                               | 3.28(3)           |
|                                | $\tilde{A}^2\Sigma^+$ |                    |                    |                              | $\nu_3(\sigma) + 2\nu_2(\pi)$ |                   |
|                                | Fit 1 <sup>a</sup>    | Fit 2 <sup>a</sup> | MRCI <sup>c</sup>  | ZEKE <sup>d</sup>            | Fit 1 <sup>a</sup>            | MRCI <sup>c</sup> |
| <i>T<sub>e</sub></i>           | 3238.8216(2)          | 3238.8224(2)       | 3233.1             | 3231                         | 3272.955(3)                   | 3269.0            |
| <i>B</i>                       | 1.39581(3)            | 1.39568(3)         | 1.3974             | 1.37(1)                      | 1.3610(1)                     | 1.3562            |
| <i>A</i>                       |                       |                    |                    |                              | -4.587(8)                     | -4.6              |
| $\gamma$                       | -0.07202(2)           | -0.07332(7)        |                    |                              |                               |                   |
| <i>p</i>                       |                       |                    |                    |                              | -0.89(2)                      |                   |
| <i>q</i>                       |                       |                    |                    |                              | 0.0034(1)                     |                   |
| <i>D</i> (× 10 <sup>-6</sup> ) | 27(1)                 | 22.7(9)            |                    |                              | 1.0(1)                        |                   |
| <i>H</i> (× 10 <sup>-7</sup> ) |                       | 70(8)              |                    |                              |                               |                   |
| $\gamma_D$                     | 0.00012(1)            | 0.000187(3)        |                    |                              |                               |                   |
|                                | $\nu_1(\sigma)$       |                    |                    | $\nu_1(\sigma) + \nu_2(\pi)$ |                               |                   |
|                                | Fit 1 <sup>a</sup>    | Rovib <sup>b</sup> | MRCI <sup>c</sup>  | Fit 1 <sup>a</sup>           | Rovib <sup>b</sup>            | MRCI <sup>c</sup> |
| <i>T<sub>e</sub></i>           | 3056.3413(2)          | 3056.3412(1)       | 3071.9             | 3340.8480(2)                 | 3340.8480(2)                  | 3352.0            |
| <i>B</i>                       | 1.34340(1)            | 1.343387(9)        | 1.3445             | 1.36993(2)                   | 1.36993(1)                    | 1.3710            |
| <i>A</i>                       | -48.5992(3)           | -48.5987(3)        | -49.1              |                              |                               |                   |
| <i>A<sub>D</sub></i>           | -0.00138(1)           | -0.001364(6)       |                    |                              |                               |                   |
| $\gamma$                       |                       |                    | -0.07294(9)        | -0.00463(5)                  | -0.00457(3)                   |                   |
| <i>p</i>                       | 0.0287(1)             | 0.02862(6)         |                    |                              |                               |                   |
| <i>q</i>                       | -0.00236(1)           | -0.002355(7)       |                    |                              |                               |                   |
| <i>D</i> (× 10 <sup>-6</sup> ) | 3.0(1)                | 2.94(7)            |                    | 2.8(4)                       | 2.8(2)                        |                   |

<sup>a</sup> Values obtained in this work. <sup>b</sup> Values taken from Ref. 4. <sup>c</sup> Values taken from Ref. 11. <sup>d</sup> Values taken from Ref. 6. <sup>e</sup> Values taken from Ref. 5.

crossing causing distortions of the experimental spectrum. It is possible that this is because the  $\tilde{A}^2\Sigma^+ \leftarrow \tilde{X}^2\Pi$  origin transition we report here is actually below the energy of the avoided crossing. We also note that this crossing is avoided while the molecule is linear (as assumed in Fig. 4), but these states may cross if the bending motion is considered. Future studies could target transitions to vibrationally excited levels of the  $\tilde{A}$  state, which are probably more dramatically perturbed by this avoided crossing. Indeed, recent work by Jusko and coworkers investigates a transition to an excited vibrational level of the  $\tilde{A}$  electronic state.<sup>45</sup>

### Hyperfine splitting

At low temperature (4 K and 9 K), the Doppler width of the lines is small enough that hyperfine splitting is observed (see Fig. 5). This splitting is on the order of 0.004 cm<sup>-1</sup> and splits most lines into three observable components. To simulate the spectrum including hyperfine splitting,  $\hat{H}_{\text{hfs}}$  was added to the Hamiltonian of eqn (1) as implemented in PGOPHER:<sup>44</sup>

$$\hat{H}_{\text{hfs}} = a\hat{I} \cdot \hat{L} + b_F\hat{I} \cdot \hat{S} + \frac{eQq_0}{4I(2I-1)}[3\hat{I}_z^2 - \hat{I}^2] \quad (2)$$

where *I* is the nuclear spin, *L* is the electronic orbital angular momentum, and *S* is the electron spin. The hyperfine constants quantify the splitting arising from coupling between the electron orbital angular momentum and the nuclear spin (*a*), the Fermi-contact parameter describing coupling between the electron spin and the nuclear spin (*b<sub>F</sub>*), and the nuclear quadrupole coupling constant (*eQq<sub>0</sub>*).<sup>46</sup> The first and second terms in eqn (2) will appear once for the splitting arising from the nitrogen nuclear spin and once for the hydrogen nuclear spin. As illustrated in Fig. 2, the nitrogen (with nuclear spin *I<sub>N</sub>* = 1) splits each *J* level into *F*<sub>1</sub> = *J* + 1, *J*, and *J* - 1. Within the coupling scheme employed here, each of these *F*<sub>1</sub> levels are split by the hydrogen (with nuclear spin *I<sub>H</sub>* = 1/2) into *F* = *F*<sub>1</sub> + 1/2 and *F* = *F*<sub>1</sub> - 1/2. However, the hyperfine splitting from the hydrogen is too small to resolve transitions to different *F* levels in our spectrum. The hyperfine structure shown in Fig. 5 is dominated by transitions with  $\Delta F_1 = 0$  and  $\Delta F = 0$ .

The experimental electronic spectrum was then refit including hyperfine coupling in PGOPHER.<sup>44</sup> This fit included lines from the pure rotational spectrum in ref. 5. This was done because fewer hyperfine constants were required to understand the hyperfine splitting for the electronic spectrum in this work



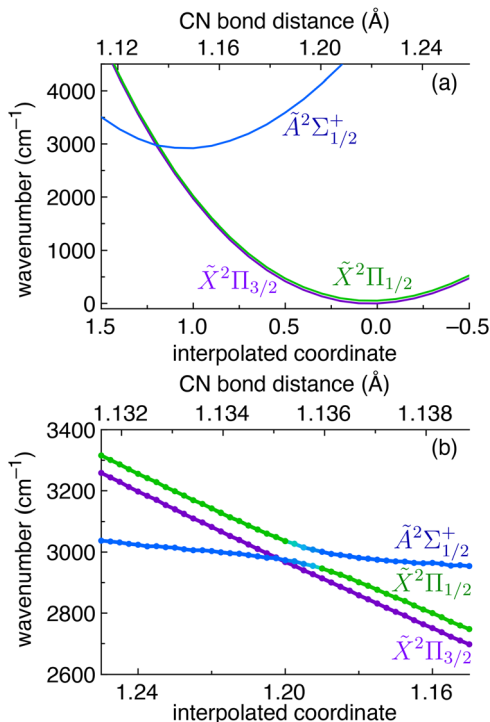


Fig. 4 (a) Potential energy surface linearly interpolating between the  $\tilde{X}^2\Pi$  and  $\tilde{A}^2\Sigma^+$  optimised geometries. An enhanced view of the avoided crossing between the  $\tilde{A}^2\Sigma_{1/2}^+$  state and the  $\tilde{X}^2\Pi_{1/2}$  component is shown in (b).

than for the pure rotational spectrum in ref. 5, and this provided a good constraint of the ground state constants. This resulted in a fit with an average residual of less than  $0.001\text{ cm}^{-1}$  and is referred to here as ‘fit 2’ in Table 2. The magnitude of the hyperfine splitting arises mostly because of the isotropic

interaction between the nuclear spin of the N atom and the electron spin in the  $\tilde{A}$  state, which is quantified by the Fermi-contact parameter  $b_F$ . This large change in  $b_F$ —five times smaller in the  $\tilde{X}$  state than the  $\tilde{A}$  state—reflects the dramatic change in the electronic structure from  $\tilde{X}$  to  $\tilde{A}$ . Therefore, the surprising fact that hyperfine splitting is resolved in these infrared spectra is definitive evidence that this is an electronic transition.

The Fermi contact parameter ( $b_F = 0.0059(1)\text{ cm}^{-1}$ ) of the N atom in the  $\tilde{A}$  state provides a direct way of quantifying the electronic wavefunctions in the  $\tilde{X}$  and  $\tilde{A}$  states. Comparing the  $b_F$  parameter in the  $\tilde{A}$  state of  $\text{HCN}^+$  with the  $b_{\text{orb}}$  of an isolated nitrogen ( $0.0514\text{ cm}^{-1}$ )<sup>12</sup> atom gives  $\frac{b_F}{b_{\text{orb}}} = 0.115$ , which means that the  $\tilde{A}$  state has only  $11.5 \pm 0.1\%$  s orbital character on the nitrogen. This is small compared to other similar nitrogen containing neutral molecules in  $^2\Sigma^+$  states.<sup>47,48</sup> The relatively low s orbital character is because the singly occupied molecular orbital resembles mostly a  $p_z$  atomic orbital on the nitrogen atom (see Fig. 1).

Another possible effect that could be lowering the percentage of s orbital character in the  $\tilde{A}\Sigma_{1/2}^+$  state could be mixing with the  $\tilde{X}\Pi_{1/2}$  state as a result of the avoided crossing in Fig. 4. This would result in the upper state having a linear combination of the  $\Sigma_{1/2}^+$  and  $\Pi_{1/2}$  state configurations. Because the  $b_F$  is five times lower in the  $\Pi$  state (see Table 2), a greater mixing between the  $\Pi$  and  $\Sigma$  configurations will reduce the  $b_F$  value in the  $\tilde{A}$  state. However, this is quite speculative, and the subtle properties of avoided crossings are challenging to calculate.

We have also calculated the  $\text{HCN}^+$  nitrogen  $b_F$  parameter of the  $\tilde{A}$  state using the equation of motion coupled cluster method EOM-CCSD/cc-pVTZ in the Gaussian/16 program.<sup>40,49–51</sup> This

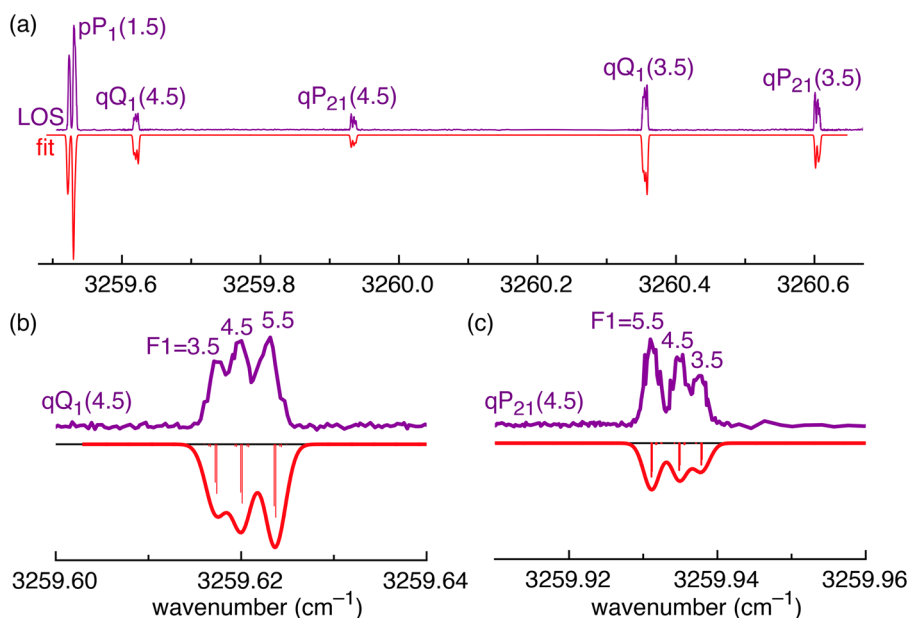


Fig. 5 (a) Portion of the  $\text{HCN}^+ \tilde{A}^2\Sigma^+ \leftarrow \tilde{X}^2\Pi$  electronic spectrum (purple trace) measured using LOS at  $\approx 9\text{ K}$  compared with a simulation (red trace) based on a contour fit using the PGOPHER program. Simulated rovibronic hyperfine transitions are shown as red sticks. The P, Q, and R branches are labelled with respect to  $\Delta N$  (lower case) and  $\Delta J$  (upper case). (b) and (c) A closer view of some of the lines shown in (a).



**Table 2** Hyperfine constants included in the line fit of a 4 K  $\tilde{A}^2\Sigma^+ \leftarrow \tilde{X}^2\Pi_{3/2}$  spectrum ( $\text{cm}^{-1}$ ). When sufficiently resolved, lines from a 35 K spectrum of the  $\tilde{A}^2\Sigma^+ \leftarrow \tilde{X}^2\Pi_{1/2}$  transition and high  $J$  lines of the  $\tilde{A}^2\Sigma^+ \leftarrow \tilde{X}^2\Pi_{3/2}$  transition were also included. Non-hyperfine constants from fit 2 are given in Table 1

|                          | $\tilde{X}^2\Pi$ | $\tilde{X}^2\Pi$ | $\tilde{A}^2\Sigma^+$ |
|--------------------------|------------------|------------------|-----------------------|
|                          | Fit 2            | Ref. 5           | Fit 2                 |
| $a(\text{N})$            | 0.0013(2)        | 0.0013(1)        |                       |
| $b_{\text{F}}(\text{N})$ | 0.0012(3)        | 0.0012(2)        | 0.0059(1)             |
| $d(\text{N})$            |                  | 0.0019(1)        |                       |
| $a(\text{H})$            | 0.0013(4)        | 0.00013(3)       |                       |
| $b_{\text{F}}(\text{H})$ | -0.00192(7)      | -0.0017(1)       | 0.0002(3)             |
| $eQq_0$                  | -0.00018(8)      | -0.00019(4)      | -0.0005(40)           |
| $eQq_2$                  |                  | -0.0005(2)       |                       |

yielded an  $\tilde{A}$  state value of  $b_{\text{F}} = 0.014 \text{ cm}^{-1}$ , which is significantly larger than the experimental value ( $b_{\text{F}} = 0.0059(1) \text{ cm}^{-1}$ ). This could be a further indication of the importance of vibronic coupling for  $\text{HCN}^+$  and suggests that the  $\tilde{A}$  state is not well described within the Born–Oppenheimer approximation.

There are very few polyatomic molecular ions for which the hyperfine structure is observed in excited electronic states. Serendipitously, one of these states is the  $\tilde{A}^2\Sigma^+$  state of  $\text{HCP}^+$ . Because phosphorus is directly below nitrogen in the periodic table, the  $\tilde{A}^2\Sigma^+$  state of  $\text{HCP}^+$  are analogous to the  $\tilde{A}^2\Sigma^+$  state of  $\text{HCN}^+$  investigated here. The  $\tilde{A}^2\Sigma^+$  state of  $\text{HCP}^+$  have a Fermi contact parameter of  $b_{\text{F}} = 0.106(5) \text{ cm}^{-1}$ , which is over an order of magnitude larger than the value we measure for  $\text{HCN}^+$  ( $b_{\text{F}} = 0.0059(1) \text{ cm}^{-1}$ ). Additionally, the  $\text{HCP}^+ \tilde{A}^2\Sigma^+$  state wavefunction has an  $s$  orbital character of 24%, which is significantly larger than that of  $\text{HCN}^+$  ( $11.5 \pm 0.1\%$ ). This might reflect a larger mixing of the phosphorous  $p_z$  and  $s$  orbitals in the highest occupied molecular  $\sigma$  orbital of  $\text{HCP}^+$  or be the result of the  $\text{HCN}^+$  avoided crossing discussed above.

A contour fit of the experimental lines in Fig. 5 was attempted to capture some of the unresolved hyperfine structure from the hydrogen nucleus; however, no significant information about the hydrogen hyperfine splitting could be observed. Nevertheless, the contour fit was used to estimate the rotational and translational ion temperature. The rotational temperature was estimated to be  $18 \pm 5 \text{ K}$  based on the relative intensities of the bands in Fig. 5, which arise from the differences in the population of the ground state  $J = 1.5, J = 3.5$ , and  $J = 4.5$  levels. The fitted Gaussian width was  $0.0020(5) \text{ cm}^{-1}$ , which corresponds to a translational temperature of  $20 \pm 5 \text{ K}$ . As expected, these values are higher than the temperature of the trap itself ( $\approx 9 \text{ K}$ ) because of RF heating.<sup>52</sup> Additionally, no Lorentzian lineshape was convoluted to account for lifetime broadening, which would further decrease the fitted Gaussian linewidth. The reason we did not include a Lorentzian in the fit is because there is considerable uncertainty in the splitting due to  $I_{\text{H}}$ , which can lead to dubious results if one attempts to interpret subtle changes in the widths of these lines. It is clear from the narrow linewidths and the fact that the individual hyperfine lines have a similar width to the rovibrational lines that the excited state has a fairly long lifetime and, therefore, the low lying avoided crossing (Fig. 4) does not lead to fast internal conversion to the ground state. Assuming a lifetime

broadening of  $0.0025 \text{ cm}^{-1}$  yields an extremely conservative lower limit for the excited state lifetime of 2 ns.

### $\Pi[\nu_3(\sigma) + 2\nu_2(\pi)]$ combination band

Although the focus of this article is the  $\tilde{A} \leftarrow \tilde{X}$  transition of  $\text{HCN}^+$ , we observed an additional vibrational transition that partially overlaps with the  $\tilde{A} \leftarrow \tilde{X}$  band, which warrants further discussion. This vibrational transition is centered around  $3295 \text{ cm}^{-1}$  and was fit with the same Hamiltonian form as described in ref. 4 (red sticks in Fig. 6). The  $P$ ,  $Q$ , and  $R$  branches are clearly apparent and feature  $\Lambda$  type doublets characteristic of a  $\Pi \leftarrow \Pi$  transition. We were unable to assign any lines associated with the  $\Pi_{1/2} \leftarrow \Pi_{\Omega}$  components. Nevertheless, the  $P$ ,  $Q$ , and  $R$  branches can only be reasonably fit to a  $\Pi \leftarrow \Pi$  transition—rather than a  $\Delta \leftarrow \Pi$  or  $\Sigma \leftarrow \Pi$  transition—and so the upper state must have  $\Pi$  vibronic symmetry.

The vibronic symmetry of  $\text{HCN}^+$  energy levels requires consideration of the Renner–Teller effect. Fig. 7 illustrates the states generated by Renner–Teller coupling in  $\text{HCN}^+$ . The vibrational angular momentum from the  $\nu_2(\pi)$  bending mode (with quantum number  $l = \nu_2, \nu_2 - 2, \dots, 0$  or 1) couples with the total electronic angular momentum (with quantum number  $\Omega$ ) to form the resulting vibronic angular momentum  $P = |\pm\Omega \pm l|$ . The quantum number  $K = |\pm\Lambda \pm l|$  results from coupling between

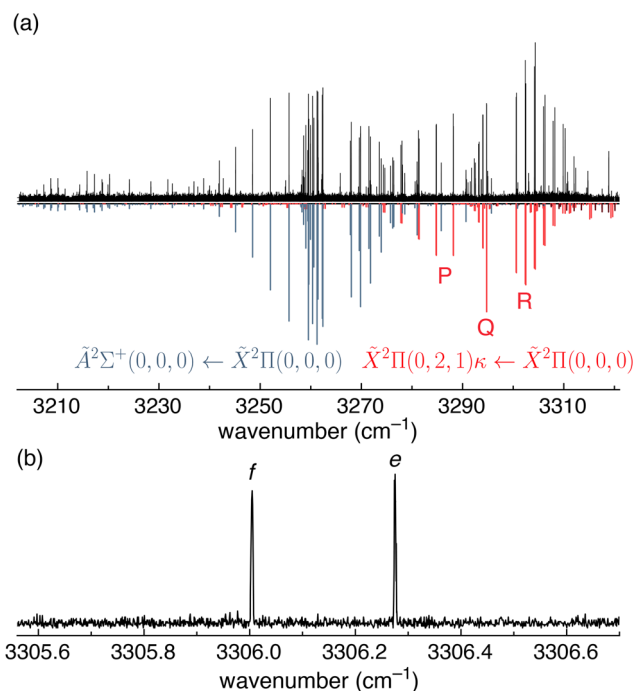


**Fig. 6** (a) Portion of the  $\text{HCN}^+ \tilde{A}^2\Sigma^+ \leftarrow \tilde{X}^2\Pi$  electronic spectrum and rovibrational spectrum exciting the  $\nu_3(\sigma) + 2\nu_2(\pi)$  combination band in the  $\tilde{X}$  ground state (black trace) measured using LOS at  $\approx 35 \text{ K}$ . The experimental spectrum is compared with a simulation of the electronic transition (grey lines) and the vibronic transition (red lines) using the PGOPHER program. The vibrational levels are labelled by  $(\nu_1, \nu_2, \nu_3)$ , which are the vibrational quantum numbers of the CH stretch ( $\nu_1$ ), the HCN bend ( $\nu_2$ ), and the CN stretch ( $\nu_3$ ). The quantum number  $\kappa$  indicates that this band is the upper Renner–Teller component for this vibration (see the term diagram in Fig. 7). (b) Example of a  $\Lambda$  doublet in the  $\nu_3(\sigma) + 2\nu_2(\pi)$  combination band spectrum.



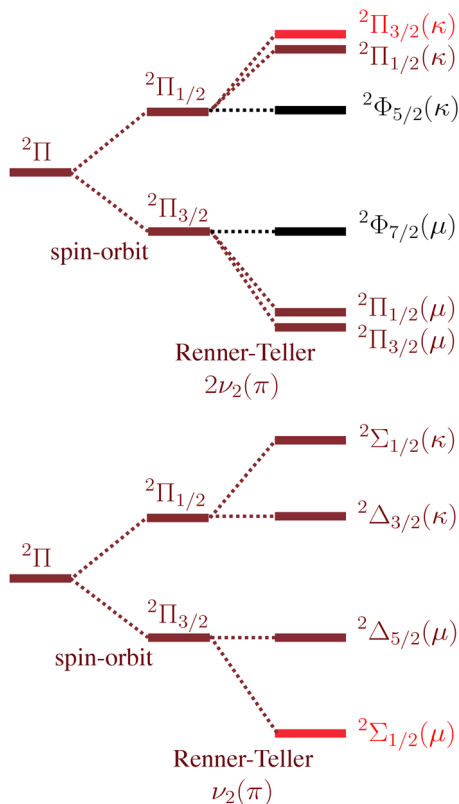


Fig. 7 Schematic illustration of the Renner–Teller splitting for the  $\tilde{X}^2\Pi$  state as a result of one (bottom) or two (top) quanta of the  $\text{HCN}^+$  bending mode  $\nu_2(\pi)$ . The term symbols on the right hand side are labelled with quantum numbers by  $^{2S+1}K_p$ . The levels observed in this study are highlighted in light red. Excitation from the ground state to levels with  $\Phi$  symmetry is forbidden, and these states are shown in black.

vibrational and orbital angular momenta. The vibronic term symbols are then  $^{2S+1}K_p$ . One quantum of the  $\nu_2(\pi)$  mode ( $l = 1$ ) couples with the orbital angular momentum ( $\Lambda = 1$ ) to generate two  $\Sigma$  and two  $\Delta$  vibronic states. Two quanta of the  $\nu_2(\pi)$  mode ( $l = 2$  and  $0$ ) couples with the orbital angular momentum  $\Lambda = 1$  to generate four  $\Pi$  and two  $\Phi$  vibronic states. The upper components are labeled  $\kappa$  and the lower components are labeled  $\mu$ .

The extracted spectroscopic constants from our fit (Table 1) agree well with the calculated values from ref. 11 for the upper ( $\kappa$ ,  $\Pi_{3/2}$ ) Renner–Teller component of the  $\nu_3(\sigma) + 2\nu_2(\pi)$  combination band, including the surprisingly low spin–orbit coupling constant ( $A_{\text{SO}} = -4.91(1) \text{ cm}^{-1}$ ). However, the  $A_{\text{SO}}$  value here only provides an effective fit, because the splitting of the  $\Pi_{p=1/2}$  and  $\Pi_{p=3/2}$  vibronic components will need to be treated different from the splitting of  $\Pi_{\Omega=1/2}$  and  $\Pi_{\Omega=3/2}$  spin–orbit components. This is consistent with the fact that transitions to  $\Pi_{p=1/2}$  levels were not observed. Considering the good agreement with calculations, we assign this band as excitation of the upper  $\kappa$ ,  $\Pi$  Renner–Teller component of the  $\nu_3(\sigma) + 2\nu_2(\pi)$  combination band ( $\Pi(0, 2, 1)\kappa$ ) as listed—but not analysed—in part I of this series of publications.<sup>4</sup>

The fact that this combination band is  $\nu_3(\sigma) + 2\nu_2(\pi)$  with  $\Pi$  symmetry validates the previous assignment in ref. 4 that a

band with  $\Sigma$  vibronic symmetry corresponds to the lower ( $\mu$ ,  $\Sigma$ ) Renner–Teller component of a  $\nu_1(\sigma) + \nu_2(\pi)$  combination band. If the  $\Sigma$  symmetry  $\nu_3(\sigma) + \nu_2(\pi)$  combination band from ref. 4 arose from the upper ( $\kappa$ ) Renner–Teller component, then one would expect to observe  $\Delta \leftarrow \Pi$  transitions slightly lower in energy. Because no such transitions are observed, the  $\Sigma$  symmetry  $\nu_3(\sigma) + \nu_2(\pi)$  combination band observed in ref. 4 can be assigned to the lower ( $\mu$ ) Renner–Teller component.

A thorough analysis of the Renner–Teller coupling of  $\text{HCN}^+$  is not within the scope of this work. Nevertheless, our results provide a promising indication that the calculations in ref. 11 are accurately capturing the strong Renner–Teller coupling of  $\text{HCN}^+$ .

The  $\Pi(0, 2, 1)\kappa$  band reported here is the first experimental spectrum of a  $\kappa$  Renner–Teller component of  $\text{HCN}^+$ . The  $\Pi(0, 2, 1)\mu$  component has been measured at  $2523 \text{ cm}^{-1}$  using ZEKE spectroscopy in ref. 6. These experimental values enable a preliminary estimate of Renner–Teller parameters of  $\text{HCN}^+$  based on only experimental values. We employed the equations describing a Renner–Teller and spin–orbit active system given in ref. 53, the fundamental vibrational frequency of the CN stretching mode  $(0, 0, 1)$  measured at  $1785 \text{ cm}^{-1}$  by Wiedmann *et al.*, and the spin–orbit constant for  $\text{HCN}^+$  determined with our high-resolution spectra ( $A_{\text{SO}} = -49.3113 \text{ cm}^{-1}$ ). From these results, we estimate an effective Renner–Teller vibrational constant of  $\omega = 580 \text{ cm}^{-1}$  and a splitting parameter of  $\varepsilon = 0.45$ . However, because of anharmonicity, these values differ from those required to fit the fundamental bending mode  $\mu$  ( $292 \text{ cm}^{-1}$ ) and  $\kappa$  components ( $821 \text{ cm}^{-1}$ ).<sup>6,11</sup>

Future high-resolution experimental studies could provide a detailed characterisation of the Renner–Teller coupling of  $\text{HCN}^+$  by combining our results with measurements of the  $\Delta(1, 1, 0)$  components and the  $\Sigma(1, 1, 0)\kappa$  component (calculated to occur at  $3881 \text{ cm}^{-1}$ ) as well as the  $\Pi(0, 2, 1)\mu$  combination band component (measured at  $2523 \text{ cm}^{-1}$  using ZEKE).<sup>6</sup> The  $\Pi(0, 2, 1)\kappa$  component in Fig. 6 is the first measured  $\kappa$  Renner–Teller component for  $\text{HCN}^+$  and serves as a valuable experimental reference point for analysing the vibronic coupling of  $\text{HCN}^+$ .

## Conclusions and outlook

In summary, we have measured high resolution electronic spectra of the infrared  $\tilde{A}^2\Sigma^+ \leftarrow \tilde{X}^2\Pi$  electronic transition origin band of  $\text{HCN}^+$ , which resolved the rotational, fine, and hyperfine structure. Although both states have been observed before, the transition between these states has never been reported, and the spectra presented here have a significantly higher resolution. Furthermore, hyperfine splitting has not been observed before and provides a lens with which the electronic wavefunction can be interrogated. In this case, we find that the  $\tilde{A}$  state electronic wavefunction has 11.5(2)%  $s$  orbital character on the N atom. The fact that we can observe hyperfine splitting in the infrared is unusual and makes it clear that the observed spectrum corresponds to an electronic transition.

The quality of these spectroscopic constants easily affords accurate simulations of the rovibronic  $\tilde{A} \rightarrow \tilde{X}$  emission of  $\text{HCN}^+$



for comparison with astronomical measurements such as those possible with the James Webb Space Telescope.<sup>54,55</sup> However, the fact that the electronic transition appears to have comparable intensity to vibrational excitation of a nearby  $\nu_3(\sigma) + 2\nu_2(\pi)$  combination band indicates that the electronic transition is fairly weak and will probably be challenging to detect astronomically.

We have recently reported electronic spectra measured using LOS with a low resolution white light fibre laser.<sup>34</sup> The electronic spectrum of  $\text{HCN}^+$  presented here illustrate that electronic transitions can be measured using LOS with a very high resolution for a mass-selected, highly reactive bare ion that is excited well below the dissociation threshold.

## Conflicts of interest

There are no conflicts to declare.

## Data availability

The datasets generated and/or analysed during the current study are available from the corresponding authors upon reasonable request.

All data supporting the findings of this study are available within the manuscript and its supplementary information (SI). Supplementary information: rovibrational scheme showing allowed rovibronic transitions and branches, the list of assigned rovibronic lines including hyperfine splitting, the list of assigned rovibronic lines from global fit without hyperfine splitting, and raw leak-out spectroscopy data for the electronic transition. See DOI: <https://doi.org/10.1039/d5cp04255k>.

## Acknowledgements

This work was supported by an ERC advanced grant (MissIons: 101020583), and the Deutsche Forschungsgemeinschaft (DFG) via Collaborative Research Center 1601 (project ID 500700252, sub-project B8 & C4) and DFG project 514067452, INST 216/1069-1 (450096019). The optical cw-OPOs were financed by DFG (INST216/1184-1, project number 504504934 and INST216/1069-1, project number 450096019). WGDPS acknowledges the Alexander von Humboldt Foundation for support through a postdoctoral fellowship.

## References

- S. Petrie, C. G. Freeman, M. Meot-Ner, M. J. McEwan and E. E. Ferguson, Experimental study of  $\text{HCN}^+$  and  $\text{HNC}^+$  ion chemistry, *J. Am. Chem. Soc.*, 1990, **112**, 7121–7126.
- P. Dohnal, P. Jusko, M. Jiménez-Redondo and P. Caselli, Measurements of rate coefficients of  $\text{CN}^+$ ,  $\text{HCN}^+$ , and  $\text{HNC}^+$  collisions with  $\text{H}_2$  at cryogenic temperatures, *J. Chem. Phys.*, 2023, **158**(24), 244303.
- D. Forney, W. E. Thompson and M. E. Jacox, The vibrational spectra of molecular ions isolated in solid neon. IX.  $\text{HCN}^+$ ,  $\text{HNC}^+$ , and  $\text{CN}^-$ , *J. Chem. Phys.*, 1992, **97**, 1664–1674.
- P. C. Schmid, S. J. P. Marlton, W. G. D. P. Silva, T. Salomon, O. Asvany and S. Schlemmer, High-resolution spectroscopy of  $[\text{H,C,N}]^+$ : I. Rotationally resolved vibrational bands of  $\text{HCN}^+$  and  $\text{HNC}^+$ , *Phys. Chem. Chem. Phys.*, 2026, DOI: [10.1039/D5CP04201A](https://doi.org/10.1039/D5CP04201A).
- W. G. D. P. Silva, P. C. Schmid, D. Gupta, S. Thorwirth, O. Asvany and S. Schlemmer, High-resolution spectroscopy of  $[\text{H,C,N}]^+$ : II. Ground state rotational spectrum of  $\text{HCN}^+$  ( $\tilde{X}^2\Pi$ ), *Phys. Chem. Chem. Phys.*, 2026, DOI: [10.1039/D5CP04204F](https://doi.org/10.1039/D5CP04204F).
- R. T. Wiedmann and M. G. White, Vibronic coupling in the  $\tilde{X}^2\Pi$  and  $\tilde{A}^2\Sigma^+$  states of  $\text{HCN}^+$ , *J. Chem. Phys.*, 1995, **102**, 5141–5151.
- A. Lorquet, J.-C. Lorquet, J. Delwiche and M.-J. Hubin-Franskin, Intramolecular dynamics by photoelectron spectroscopy. I. Application to  $\text{N}_2^+$ ,  $\text{HBr}^+$ , and  $\text{HCN}^+$ , *J. Chem. Phys.*, 1982, **76**, 4692–4699.
- C. Fridh and L. Åsbrink, Photoelectron and electron impact spectrum of  $\text{HCN}$ , *J. Electron Spectrosc. Relat. Phenom.*, 1975, **7**, 119–138.
- J. Hollas and T. Sutherley, Geometry of  $\text{C}_2\text{N}_2^+$  and  $\text{HCN}^+$  from low-energy photoelectron spectroscopy, *Mol. Phys.*, 1972, **24**, 1123–1131.
- J. Eland, T. Field, P. Baltzer and D. Hirst, Photoelectron spectra, electronic structure, coincidence spectra and dissociation mechanisms of the hydrogen cyanide cation, *Chem. Phys.*, 1998, **229**, 149–163.
- R. Tarroni, A. Mitrushenkov, P. Palmieri and S. Carter, Energy levels of  $\text{HCN}^+$  and  $\text{DCN}^+$  in the vibronically coupled  $\tilde{X}^2\Pi$  and  $\tilde{A}^2\Sigma^+$  states, *J. Chem. Phys.*, 2001, **115**, 11200–11212.
- J. A. Fitzpatrick, F. R. Manby and C. M. Western, The interpretation of molecular magnetic hyperfine interactions, *J. Chem. Phys.*, 2005, **122**(8), 084312.
- M. Nötzold, R. Wild, C. Lochmann and R. Wester, Spectroscopy and ion thermometry of C 2- using laser-cooling transitions, *Phys. Rev. A*, 2022, **106**, 023111.
- I. Dabrowski and G. Herzberg, The spectrum of  $\text{HeNe}^+$ , *J. Mol. Spectrosc.*, 1978, **73**, 183–214.
- A. Carrington, D. R. Milverton and P. J. Sarre, Electronic absorption spectrum of  $\text{CO}^+$  in an ion beam: Analysis of the carbon nuclear hyperfine structure in  $^{13}\text{CO}^+$ , *Mol. Phys.*, 1978, **35**, 1505–1521.
- P. J. Sarre, J. M. Walmsley and C. J. Whitham, High-resolution laser photofragment spectroscopy of  $\text{CH}^+$ , *J. Chem. Soc., Faraday Trans. 2*, 1986, **82**, 1243–1255.
- P. Sarre, J. Walmsley and C. Whitham, Laser photofragment spectroscopy of near-threshold resonances in  $\text{SiH}^+$ , *Philos. Trans. R. Soc., A*, 1988, **324**, 233–246.
- C. Edwards, C. Maclean and P. Sarre, Laser predissociation spectrum of  $\text{SH}^+$  ( $\tilde{A}^3\Pi-X^3\Sigma^-$ ) Analysis of proton hyperfine structure, *Mol. Phys.*, 1984, **52**, 1453–1466.
- C. Edwards, P. Jackson, P. Sarre and D. Milton, Laser photofragment and emission spectroscopy of the  $\tilde{A}^2\Delta-X^2\Pi$  system of  $\text{PH}^+$ , *Mol. Phys.*, 1986, **57**, 595–604.
- P. Cosby, H. Helm and M. Larzilliere, Photofragment spectroscopy of  $\text{HF}^+$ , *J. Chem. Phys.*, 1991, **94**, 92–105.
- K. Boudjarane, J. Lacoursière and M. Larzillière, Hyperfine structure of first negative system ( $\tilde{B}^2\Sigma_u^+-X^2\Sigma_g^+$ ) of  $^{14}\text{N}_2^+$  and  $^{15}\text{N}_2^+$  from laser-induced fluorescence measurements, *J. Chem. Phys.*, 1994, **101**, 10274–10282.



- 22 M. Larzilli re, S. Abed, M. Carr e, M. Gaillard, J. Lerm e and M. Broyer, I-Type doubling hyperfine structure of  $N_2O^+$ , *Chem. Phys. Lett.*, 1985, **119**, 55–60.
- 23 F. X. Sunahori, X. Zhang and D. J. Clouthier, Electronic spectroscopy of jet-cooled  $HCP^+$ : Molecular structure, phosphorus hyperfine structure, and Renner-Teller analysis, *J. Chem. Phys.*, 2007, **127**(10), 104312.
- 24 H.-W. H ubers, K. M. Evenson, C. Hill and J. M. Brown, The rotational spectrum of the  $NH^+$  radical in its  $X^2\Pi$  and  $a^4\Sigma^-$  states, *J. Chem. Phys.*, 2009, **131**(3), 034311.
- 25 G. A. Pino, G. Feraud, M. Broquier, G. Gr egoire, S. Soorkia, C. Dedonder and C. Jovet, Non-radiative processes in protonated diazines, pyrimidine bases and an aromatic azine, *Phys. Chem. Chem. Phys.*, 2016, **18**, 20126–20134.
- 26 D. Bomse, R. Woodin and J. Beauchamp, Molecular activation with low-intensity CW infrared laser radiation. Multiphoton dissociation of ions derived from diethyl ether, *J. Am. Chem. Soc.*, 1979, **101**, 5503–5512.
- 27 Y. Zhao, E. de Beer, C. Xu, T. Taylor and D. M. Neumark, Spectroscopy and electron detachment dynamics of  $C_4^-$ ,  $C_6^-$ , and  $C_8^-$ , *J. Chem. Phys.*, 1996, **105**, 4905–4919.
- 28 T. Salomon, S. Brackertz, O. Asvany, I. Savi c, D. Gerlich, M. E. Harding, F. Lipparini, J. Gauss, A. van der Avoird and S. Schlemmer, The  $He-H_3^+$  complex. II. Infrared predissociation spectrum and energy term diagram, *J. Chem. Phys.*, 2022, **156**(14), 144308.
- 29 S. J. Marlton, J. T. Buntine, P. Watkins, C. Liu, U. Jacovella, E. Carrascosa, J. N. Bull and E. J. Bieske, Probing colossal carbon rings, *J. Phys. Chem. A*, 2023, **127**, 1168–1178.
- 30 T. E. Douglas-Walker, E. K. Campbell, F. C. Daly, S. Douin, B. Gans, U. Jacovella, C. Maurice, R. Odant and J. Palotas, Ion Spectroscopy in the Context of the Diffuse Interstellar Bands: A Case Study with the Phenylacetylene Cation, *ACS Earth Space Chem.*, 2024, **8**(12), 2644–2651.
- 31 S. Schlemmer, T. Kuhn, E. Lescop and D. Gerlich, Laser excited  $N_2^+$  in a 22-pole ion trap: Experimental studies of rotational relaxation processes, *Int. J. Mass Spectrom.*, 1999, **185**, 589–602.
- 32 S. Chakrabarty, M. Holz, E. K. Campbell, A. Banerjee, D. Gerlich and J. P. Maier, A novel method to measure electronic spectra of cold molecular ions, *J. Phys. Chem. Lett.*, 2013, **4**, 4051–4054.
- 33 P. C. Schmid, O. Asvany, T. Salomon, S. Thorwirth and S. Schlemmer, Leak-out spectroscopy, a universal method of action spectroscopy in cold ion traps, *J. Phys. Chem. A*, 2022, **126**, 8111–8117.
- 34 S. J. Marlton, P. C. Schmid, T. Salomon, O. Asvany and S. Schlemmer, Measuring Electronic Transitions Using Leak-Out Spectroscopy, *J. Phys. Chem. Lett.*, 2025, **16**, 8758–8763.
- 35 S. Schlemmer, E. Lescop, J. von Richthofen, D. Gerlich and M. A. Smith, Laser induced reactions in a 22-pole ion trap:  $C_2H_2^+ + h\nu \rightarrow C_2H_3^+ + H$ , *J. Chem. Phys.*, 2002, **117**, 2068–2075.
- 36 O. Asvany, F. Biela, D. Moratschke, J. Krause and S. Schlemmer, Note: New design of a cryogenic linear radio frequency multipole trap, *Rev. Sci. Instrum.*, 2010, **81**(7), 076102.
- 37 N. Daly, Scintillation type mass spectrometer ion detector, *Rev. Sci. Instrum.*, 1960, **31**, 264–267.
- 38 O. Asvany, S. Br unken, L. Kluge and S. Schlemmer, COLTRAP: a 22-pole ion trapping machine for spectroscopy at 4 K, *Appl. Phys. B: Lasers Opt.*, 2014, **114**, 203–211.
- 39 K. Andersson, P. A. Malmqvist, B. O. Roos, A. J. Sadlej and K. Wolinski, Second-order perturbation theory with a CASSCF reference function, *J. Phys. Chem.*, 1990, **94**, 5483–5488.
- 40 T. H. Dunning Jr, Gaussian basis sets for use in correlated molecular calculations. I. The atoms boron through neon and hydrogen, *J. Chem. Phys.*, 1989, **90**, 1007–1023.
- 41 I. Fdez Galvan, M. Vacher, A. Alavi, C. Angeli, F. Aquilante, J. Autschbach, J. J. Bao, S. I. Bokarev, N. A. Bogdanov and R. K. Carlson, *et al.*, OpenMolcas: From source code to insight, *J. Chem. Theory Comput.*, 2019, **15**, 5925–5964.
- 42 P. J. Knowles and H.-J. Werner, An efficient method for the evaluation of coupling coefficients in configuration interaction calculations, *Chem. Phys. Lett.*, 1988, **145**, 514–522.
- 43 F. Neese, Software update: The ORCA program system–Version 5.0, *Wiley Interdiscip. Rev.: Comput. Mol. Sci.*, 2022, **12**, e1606.
- 44 C. M. Western, PGOPHER: A program for simulating rotational, vibrational and electronic spectra, *J. Quant. Spectrosc. Radiat. Transfer*, 2017, **186**, 221–242.
- 45 M. Jim enez-Redondo; C. Schleif; J. Palot s; J. Sarka; H. Bunn; P. Dohnal; C. Paola and P. Jusko, High Resolution Overtone Spectroscopy of  $HCN^+$  and  $HNC^+$ . *Submitted*, 2025.
- 46 R. A. Frosch and H. Foley, Magnetic hyperfine structure in diatomic molecules, *Phys. Rev.*, 1952, **88**, 1337.
- 47 T. Suzuki, S. Saito and E. Hirota, Hyperfine coupling constants of  $NCO$  in  $\tilde{A}^2\Sigma^+$  by sub-Doppler spectroscopy, *J. Mol. Spectrosc.*, 1986, **120**, 414–420.
- 48 H. Radford, Hyperfine Structure of the  $B^2\Sigma^+$  State of  $CN$ , *Phys. Rev.*, 1964, **136**, A1571.
- 49 M. J. Frisch; G. W. Trucks; H. B. Schlegel; G. E. Scuseria; M. A. Robb; J. R. Cheeseman; G. Scalmani; V. Barone; G. A. Petersson; H. Nakatsuji; *et al.* *Gaussian 16 Revision C.01.*, 2016, Gaussian Inc., Wallingford CT, 2009.
- 50 H. Koch and P. J rgensen, Coupled cluster response functions, *J. Chem. Phys.*, 1990, **93**, 3333–3344.
- 51 J. F. Stanton and R. J. Bartlett, The equation of motion coupled-cluster method. A systematic biorthogonal approach to molecular excitation energies, transition probabilities, and excited state properties, *J. Chem. Phys.*, 1993, **98**, 7029–7039.
- 52 O. Asvany and S. Schlemmer, Numerical simulations of kinetic ion temperature in a cryogenic linear multipole trap, *Int. J. Mass Spectrom.*, 2009, **279**, 147–155.
- 53 G. Herzberg, *Molecular Spectra and molecular structure-Vol III*, Read Books Ltd, 2013, vol. 1.
- 54 P. B. Changala, N. L. Chen, H. L. Le, B. Gans, K. Steenbakkens, T. Salomon, L. Bonah, I. Schroetter, A. Canin and M.-A. Martin-Drumel, *et al.*, Astronomical  $CH_3^+$  rovibrational assignments-A combined theoretical and experimental study validating observational findings in the d203-506 UV-irradiated protoplanetary disk, *Astron. Astrophys.*, 2023, **680**, A19.
- 55 O. Bern e, M.-A. Martin-Drumel, I. Schroetter, J. R. Goicoechea, U. Jacovella, B. Gans, E. Dartois, L. H. Coudert, E. Bergin and F. Alarcon, *et al.*, Formation of the methyl cation by photochemistry in a protoplanetary disk, *Nature*, 2023, **621**, 56–59.

